Journal of Materials Chemistry A

Microwave-Assisted Growth of In2O3 Nanoparticles on WO3 Nanoplates to Improve H2S-Sensing Performance

Journal:	*Journal of Materials Chemistry A*
Manuscript ID:	TA-ART-07-2014-003426.R1
Article Type:	Paper
Date Submitted by the Author:	29-Aug-2014

Complete List of Authors:	Yin, Li; Zhengzhou University, School of Materials and Engineering Chen, Deliang; Zhengzhou University, School of Materials Science and Engineering Hu, Mingxiang; Zhengzhou University, School of Materials and Engineering Shi, Haiyue; Zhengzhou University, School of Materials and Engineering Yang, Dewei; Zhengzhou University, School of Materials and Engineering Fan, Bingbing; Zhengzhou University, School of Materials and Engineering Shao, Gang; Zhengzhou University, School of Materials and Engineering Zhang, Rui; Zhengzhou University, School of Materials and Engineering Shao, Guosheng; Zhengzhou University, School of Materials Science and Engineering; University of Bolton, Institute for Renewable Energy and Environmental Technologies

Graphical abstract：

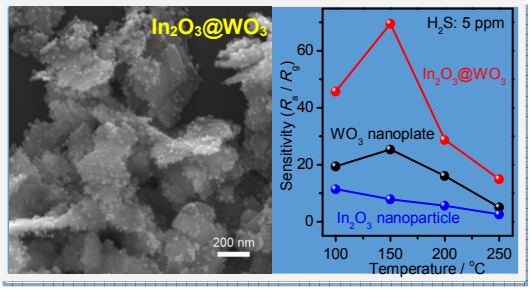

Text：

In_2O_3@WO_3 composites, synthesized via a microwave-assisted method, show high sensitive to H_2S for the synergistic effect of In_2O_3 and WO_3.

Microwave-Assisted Growth of In_2O_3 Nanoparticles on WO_3 Nanoplates to Improve H_2S-Sensing Performance

Li Yin [a], Deliang Chen [a, *], Mingxiang Hu [a], Haiyue Shi [a], Dewei Yang [a], Bingbing Fan [a], Gang Shao [a], Rui Zhang [a, b, *], Guosheng Shao [a, c]

[a] *School of Materials Science and Engineering, Zhengzhou University, 100 Science Road, Zhengzhou 450001, P.R.China*

[b] *Laboratory of Aeronautical Composites, Zhengzhou Institute of Aeronautical Industry Management, University Centre, Zhengdong New District, Zhengzhou 450046, China*

[c] *Institute for Renewable Energy and Environmental Technology, University of Bolton, Bolton BL3 5AB, UK*

***Corresponding author*:**

School of Materials Science and Engineering, Zhengzhou University, 100 Science Road, Zhengzhou 450001, P.R. China

E-mail address: dlchen@zzu.edu.cn (D.L. Chen) and zhangray@zzu.edu.cn (R. Zhang)

Tel: +86-371-67781046 Fax: +86-371-67781593

Abstract

Hierarchical In_2O_3@WO_3 nanocomposites, consisting of discrete In_2O_3 nanoparticles (NPs) on single-crystal WO_3 nanoplates, were synthesized via a novel microwave-assisted growth of In_2O_3 NPs on the surfaces of WO_3 nanoplates that were derived through an intercalation and topochemical-conversion route. The techniques of XRD, SEM, TEM and XPS were used to characterize the samples obtained. The gas-sensing properties of In_2O_3@WO_3 nanocomposites, together with WO_3 nanoplates and In_2O_3 nanoparticles, were comparatively investigated using inorganic gases and organic vapors as the target substances, with an emphasis on H_2S-sensing performance under low concentrations (0.5–10 ppm) at 100–250 ^oC. The results show that the In_2O_3 NPs with a size range of 12-20 nm are uniformly anchored on the surfaces of the WO_3 nanoplates. The amounts of the In_2O_3 NPs can be controlled by changing the In^{3+} concentrations in their growth precursors. The In_2O_3@WO_3(In/W=0.8) sample has highest H_2S-sensing performance operating at 150 ^oC: its response to 10 ppm H_2S is as high as 143, 4 times higher than that of WO_3 nanoplates and 13 times that of In_2O_3 nanocrystals. However, the responses of the In_2O_3@WO_3 sensors are less than 13 upon exposure to 100 ppm of CO, SO_2, H_2, CH_4 and organic vapors, operating at 100–150 ^oC. The improvement in response and selectivity of the In_2O_3@WO_3 sensors upon exposure to H_2S molecules can be attributed to the synergistic effect of In_2O_3 NPs and WO_3 nanoplates: hierarchical microstructures and multifunctional interfaces.

1. Introduction

Gas sensors based on metal oxide semiconductors (MOSs) have important and extensive applications in industries and environmental control.[1-3] Due to high surface areas and less agglomerated configuration, hierarchically functional MOS-based nanostructures are the hot focus in fundamental research for high-performance gas-sensing applications.[4] Recently, various hierarchical MOS nanostructures have been designed to make gas sensors.[5-10] Among them, hierarchical binary oxide nanocomposites can provide abundant physical and chemical properties, and can be expected to earn enhanced gas-sensing properties.[11] For the considerations of steric effect and specific surface areas, one-dimensional (1D) and two-dimensional (2D) nanostructures can be excellent components, which can support functional zero-dimensional (0D) nanoparticles to construct hieratical nanocomposites. Some hierarchical 0D/1D nanostructures, including SnO_2/α-Fe_2O_3 nanotubes,[12] In_2O_3/SnO_2 nanorods,[13] CuO/ZnO nanorods[14] and NiO/ZnO nanotubes,[15] have been reported for gas-sensing applications. Comparatively, relatively few hierarchical 0D/2D binary oxide nanostructures have been reported.[16]

Chemists and materials scientists have made great efforts to achieve hierarchical binary oxide nanocomposites with sophisticated microstructures.[16-26] In general, there are two strategies for the synthesis of binary oxide nanocomposites. One is one-step processes including coprecipitation,[13,17] hydrothermal,[18] electrospinning[15] and sol-gel methods.[19] The other is multiple-step (or step-by-step) processes, which have been widely developed to synthesize hierarchical nanocomposites, including ZnO-In_2O_3,[21] Fe_2O_3/WO_3[22] and α-Fe_2O_3/ZnO.[24] In the two-step growth procedure, as an effective approach, in-situ growth of second phase has been used for 1D oxide-based composite. Xue et al.[26] reported gas sensors with 1D CuO nanoparticles/SnO_2 nanorods PN-junctions and their sensitivity against 10 ppm H_2S at 60 ^oC is up to 9.4×10^6. However, those multiple-step processes developed are complicated and difficult to achieve controllable synthesis and efficient control in morphologies. Simple and efficient processes for constructing hierarchical MOS nanostructures are urgent. Microwave heating technology has been used to prepare inorganic materials because of relatively low cost and high efficiency, particularly for the fine control

over the structure, size and morphology. Microwave-assisted technology is thus an effective way for the fabrication of hierarchical MOS nanostructures. [27]

WO_3 and In_2O_3 are n-type semiconductors, and their nanomaterials have been widely investigated as gas-sensing materials. The sensors based on WO_3 nanocrystals are highly sensitive to reducing gases (e.g., H_2S and H_2) and oxidizing gases (e.g., NO and NO_2).[28-30] Two-dimensional WO_3 nanocrystals are particularly suitable for gas-sensing applications.[31,32] Kida et al.[16] introduced SnO_2 nanoparticles into WO_3 lamella-based films by mixing two suspensions containing $WO_3 \cdot nH_2O$ and SnO_2 nanoparticles, respectively, and the effective insertion of nanoparticles into WO_3 lamella stacks improved the porosity and sensitivity. But the SnO_2 nanoparticles were not evenly distributed on the surface of WO_3 lamella. In_2O_3 is also a promising gas-sensing material especially to detect H_2S.[33-39] The combination of WO_3 and In_2O_3 nanocrystals, i.e., In_2O_3/WO_3 composite, can be expected to be an efficient gas-sensing system for gas detection. But the In_2O_3/WO_3 composites reported were fabricated by simply mixing the solid-state precursor powders.[40,41] The microstructural control of the second phase is not available, and it is still a big challenge to achieve hierarchical In_2O_3/WO_3 nanocomposites.

In this work, we develop a simple microwave-assisted process to grow In_2O_3 nanoparticles (NPs) on the surfaces of WO_3 nanoplates, forming a hierarchical $In_2O_3@WO_3$ nanocomposite that is sensitive for gas detection. Two-dimensional WO_3 nanoplates are synthesized according to the intercalation and topochemical conversion process developed previously.[42] The WO_3 nanoplates have a high diameter-to-thickness ratio and single-crystalline structure, suitable as an efficient substrate to form hierarchical nanocomposites.[43] The In_2O_3 NPs are in-situ formed on the surfaces of WO_3 nanoplates during the microwave heating and the followed calcination. Using the WO_3 nanoplates as substrates, the monodispersed In_2O_3 NPs are separately anchored on the WO_3 surfaces to form hierarchical $In_2O_3@WO_3$ nanocomposites. The hierarchical $In_2O_3@WO_3$ nanostructures not only can prevent the aggregation of the In_2O_3 NPs with small particle sizes, but also can provide a special porous microstructure for the efficient diffusion and adsorption of gas molecules during the gas detection.

The simple microwave-assisted process developed here offers several advantages in the

fabrication of hierarchical 0D/2D binary oxide nanostructures. The reaction time for the formation of $In(OH)_3$ NPs is as short as 5 min. The reaction temperature is lower than 100 ^oC and there is no high pressure. The WO_3 nanoplates can be kept stable during the rapid reaction even in an alkaline condition. In addition, the microwave process may promote the heterogeneous nucleation of $In(OH)_3$ NPs on the surfaces of WO_3 nanoplates due to selective absorption of microwave energy, leading to the uniform distribution of In_2O_3 NPs on WO_3 nanoplates. The gas-sensing properties of the In_2O_3@WO_3 nanocomposites were comparatively tested, with an emphasis on the H_2S detection. The effects of In_2O_3 amounts and operating temperatures on their H_2S-sensing performances and the related mechanisms were carefully investigated.

2. Experimental section

2.1. Synthesis of WO_3 nanoplates

WO_3 nanoplates were synthesized according to our previously reported method involving an intercalation and topochemical conversion process.[42,44] Briefly, tungstic acid (5.8 g) was dispersed in a mixture of *n*-octylamine (50 cm^3) and heptane (350 cm^3) at room temperature, and kept magnetically stirring for 72 h to form tungstate-based inorganic-organic hybrid belts. The hybrid belts were dried at room temperature and then dispersed in a HNO_3 aqueous solution (~38%) and magnetically stirred for 48 h, and a yellowish suspension was obtained. The yellowish precipitates were washed with water and ethanol for about 4 times, and dried at 100 ^oC for 12 h. The dried product was H_2WO_4 nanoplates. Finally, the as-obtained H_2WO_4 nanoplates were calcined at 400 ^oC for 2 h to obtain WO_3 nanoplates.

2.2. Synthesis of In_2O_3@WO_3 nanocomposites

The In_2O_3@WO_3 nanocomposites were fabricated via a microwave-assisted heating method. Typically, for the In_2O_3@WO_3 (In/W=0.5) composite with the molar In/W ratio of 0.5, 0.1 g of WO_3 nanoplates were dispersed in 60 mL distilled water in a conical flask under an ultrasonic treating for 30 min. Polyvinylpyrrolidone K30 (PVP, 0.028 g), $In(NO_3)_3 \cdot 4.5H_2O$ (0.08 g) and urea (0.025 g) were then added to the above WO_3 suspension in order, followed by magnetically stirring for 60 min, 60 min and 30 min, respectively. The molar ratio of PVP

units to $In(NO_3)_3$ was ~1.2, and the molar ratio of urea to $In(NO_3)_3$ was ~2. The as-obtained mixture was then placed in a microwave oven (600 W, 2.45 GHz, XO-SM100, Nanjing Xian'ou Instrument Manufacturing Co. Ltd) and heated for 5 min. It is noted that the used microwave oven has a maximum power of 1000 W, and there is no special requirements in the microwave heating process. After cooled down in an ice bath, the yellowish precipitates were collected, washed with distilled water and ethanol, and then dried in a vacuum oven at 60 ^oC for 12 h. Finally, the In_2O_3@WO_3 nanocomposites were obtained by calcining the yellowish precipitates in air at 550 ^oC for 5 h. For the purpose of comparisons, other samples with various amounts of In_2O_3 species, i.e., In_2O_3@WO_3(In/W=0.8) and In_2O_3@WO_3(In/W=1) were also synthesized using the similar process.

2.3. Synthesis of In_2O_3 nanocrystals

In_2O_3 nanocrystals were also synthesized for comparison purpose. $In(NO_3)_3 \cdot 4.5H_2O$ (0.4 g) and urea (0.125 g) were dissolved in 60 mL water. After stirring for 30 min, the mixture solution was treated for 5 min in a microwave oven (600 W, 2.45 GHz) and then transferred into a 100 ml teflon lined stainless autoclave. The autoclave was sealed and maintained at 150 ^oC for 4 h. The resulting product was centrifuged and washed with water for three times, and then dried at 60 ^oC overnight. Finally, the In_2O_3 nanoparticles were obtained by calcining the above white precipitate in air at 550 ^oC for 5 h.

2.4 Characterization of compositions and microstructures

The phases of the WO_3 nanoplates, In_2O_3 nanocrystals and In_2O_3@WO_3 nanocomposite obtained were analyzed using a Rigaku D/Max-3B X-ray diffractometer with Cu Kα radiation (XRD, λ = 0.15406 nm). Their morphology and microstructures were determined on a scanning electron microscope (SEM, JEOL JSM-5600, Japan) with an acceleration voltage of 15 kV, and on a transmission electron microscope (TEM, FEI Tecnai-G2, USA) with an acceleration voltage of 200 kV. The Brunauer-Emmett-Teller (BET) surface area was tested using a Quantachrome Nova2000 sorption analyzer. The XPS spectra were recorded on a multipurpose X-ray photoelectron spectroscope (Kratos Amicus, Manchester, UK) with a

microfocused monochromatic X-ray source of Al Kα, using adventitious carbon (C1s 284.8 eV) as the calibration reference.

2.5 Sensor fabrication and gas-sensing test

For the sensor fabrication, the In_2O_3@WO_3 powders (or WO_3 nanoplates, In_2O_3 nanocrystals) were mixed with a small amount of ethanol to form a paste. Then the paste was coated onto the surface of an Al_2O_3 tube to form a continuous thin film. The as-obtained sensors were heated at 300 °C for 5 h in air before the gas-sensing test.

The gas-sensing test was carried out on a commercially available WS-30A measurement system. The testing system was placed in a ventilating cabinet with a large draught capacity. The sensor (R) is connected in series with a load resistor (R_0) with a known resistance (100–20000 KΩ), and a fixed source voltage (U_0) of 5 V is loaded on the circuit. The system measured the voltages (U) loaded on the resistor R_0, and the resistances (R) of the In_2O_3-WO_3 sensors can therefore be calculated[45]: $R = (5-U)\bullet R_0/U$. The sensor response (S_r) of a gas sensor based on *n*-type semiconductors can be described as $S_r = R_a/R_g$ for reducing gases and $S_r = R_g/R_a$ for oxidizing gases, where R_a is the sensor resistance in air and R_g is the sensor resistance in target gas. The response (or recovery) time is defined as the time in reaching 90% of the saturated value of sensor resistance in (or off) the presence of target gas. [43,46]

The harmful, flammable gases (*e.g.*, H_2S, CH_4, CO, H_2 and SO_2) and some common organic vapors (*e.g.*, methanol, ethanol, isopropanol, methanal, acetone and benzene) were chosen as the target substances to evaluate the gas-sensing performances of the WO_3, In_2O_3 and In_2O_3@WO_3 sensors. The H_2S detection was operated at 100–250 ^oC with [H_2S] = 0.5–10 ppm, while the other gases with a concentration of 100 ppm were tested at 150 ^oC.

3. Results and discussion

3.1. Phases and microstructures

In_2O_3@WO_3 nanocomposites were synthesized via a microwave-assisted method. In^{3+}-PVP@WO_3 species were firstly formed by adsorbing In^{3+} ions to the surface of WO_3 nanoplates with the assistance of PVP molecules. Urea was hydrolyzed to produce OH- species at ~80 ^oC under the microwave heating. In^{3+}-PVP@WO_3 then reacted with OH^- to

form $In(OH)_3@WO_3$. Finally, the $In_2O_3@WO_3$ nanocomposites were obtained by calcining the $In(OH)_3@WO_3$ at 550 ^oC for 5 h in air.

Fig. 1.

The phase compositions of the WO_3, In_2O_3 and $In_2O_3@WO_3$ composite were examined by XRD (Fig. 1). Fig. 1a shows the pure In_2O_3 nanocrystals obtained through the hydrothermal route, and the sample consists of the cubic In_2O_3 phase (JCPDS 06-0416, Fig. 1d). Fig. 1c shows the typical XRD pattern of the WO_3 nanoplates, which can be readily indexed to a triclinic WO_3 phase according to the literature (JCPDS card no. 32-1395, Fig. 1e). It is notable that the intensity ratio (I_{002} / I_{200}) of (002) to (200) reflections of the as-obtained WO_3 nanoplates is ~ 3.0, much higher than that (~ 0.85) of the literature data, indicating that the WO_3 sample obtained takes on a strong preferred orientation, and the (002) crystal planes have larger possibility to reflect than others. The lattice parameters of the WO_3 and In_2O_3 samples were refined based on their XRD patterns using a UnitCell program (a method developed by TJB Holland and SAT Redfern). The refined results show that the lattice parameters (a = ~7.304 Å, b = ~7.515 Å, c = ~7.682 Å, α = ~88.85^o, β = ~90.87^o, γ = ~90.86^o) of the WO_3 samples are close to those (a = 7.309 Å, b = 7.522 Å, c = 7.678 Å, α = 88.81^o, β = 90.92^o, γ = 90.93^o) of the triclinic WO_3 phase according to the literature data (JCPDS card no. 32-1395). The lattice parameter (a = ~10.113 Å) of the In_2O_3 samples are close to that (10.118 Å) of the cubic In_2O_3 phase according to the literature data (JCPDS card no. 06-0416). The XRD pattern of $In_2O_3@WO_3$(In/W=0.8) is shown in Fig. 1b, and it is the combination of crystalline WO_3 and In_2O_3 species, confirming the formation of the $In_2O_3@WO_3$ composites.

Fig. 2.

The morphology and microstructure of the samples were observed by SEM and TEM (Fig. 2 and Fig. 3). Fig. 2a shows the SEM image of the WO_3 nanoplates. One can find that the WO_3 sample mainly consists of nanoplates with an edge-length range of 200–600 nm and thicknesses of about 10–30 nm. Fig. 2b shows the SEM image of the pure In_2O_3 nanoparticles. The size of the cubic In_2O_3 particles is about 30-80 nm, besides some large blocks with sizes over 100 nm. Fig. 2c, d and e show the SEM images of the $In_2O_3@WO_3$(In/W=0.5), $In_2O_3@WO_3$(In/W=0.8) and $In_2O_3@WO_3$(In/W=1) composites, respectively. The small particles attached on the surface of WO_3 nanoplates should be the In_2O_3 NPs. When the

apparent In/W ratios of In_2O_3@WO_3 nanocomposites increase from 0.5 to 1, the mean particle sizes of the In_2O_3 NPs in the In_2O_3@WO_3 nanocomposites increase from ~15 nm to ~36 nm, and the number density also increases. The EDS spectrum of the In_2O_3@WO_3(In/W=0.8) composite in Fig. 2f indicates that the sample consists of elemental W, In and O, agreeing with the XRD result (Fig. 1b).

Fig. 3.

Fig. 3 shows the typical TEM images of the In_2O_3@WO_3(In/W=0.8) sample. The low-magnification TEM image shown in Fig. 3a indicates that the In_2O_3 NPs are uniformly and tightly immobilized on the surface of WO_3 nanoplates, and their particle size is about 10-20 nm, similar to the SEM observation. The high-resolution TEM image is shown in Fig. 3b. The crystalline interplanar spacing of 0.376 nm and 0.292 nm are corresponding to the (020) planes of WO_3 and (222) planes of In_2O_3, respectively, indicating that the In_2O_3 NPs are formed directly on the crystal plane of the WO_3 nanoplates.

Fig. 4.

The chemical composition of the In_2O_3@WO_3 sample was determined by XPS spectra. Fig. 4 shows the typical XPS spectra of the In_2O_3@WO_3(In/W=0.8) nanocomposite. Fig. 4a shows the survey spectrum, suggesting that the sample consists of W, In, O and C. the elements of W, In and O belong to the In_2O_3@WO_3 sample, and the elemental C can be due to the carbon tape used to attach the sample powders during the XPS measurement. The W 4f spectrum shown in Fig. 4b has two obvious peaks at 35.3 and 37.4 eV, belonging to $W4f_{7/2}$ and $W4f_{5/2}$ of WO_3, respectively.[43] The In 3d spectrum is shown in Fig. 4c, consisting of a single doublet at binding energies of 452.2 eV for In $3d_{3/2}$ and 444.6 eV for In $3d_{5/2}$.[47] Fig. 4d shows the O 1s spectrum. There are two peaks at 530.3 and 532.1 eV. The intense peak at 530.3 eV can be assigned to lattice oxygen in WO_3 and In_2O_3 species, and the weak peak at 532.1 eV should due to the adsorbed oxygen.[48] Taking the results of XRD patterns (Fig. 1), SEM (Fig. 2) and TEM images (Fig. 3) and XPS spectra (Fig. 4) into account, we can safely conclude that the In_2O_3@WO_3 nanocomposite consists of cubic In_2O_3 NPs and triclinic WO_3 nanoplates, and that the In_2O_3 NPs are uniformly anchored on the surfaces of the WO_3 nanoplates.

Fig. 5.

Nitrogen adsorption–desorption analysis was conducted to check the specific surface areas of the samples. Fig. 5 shows the typical the nitrogen (N_2) adsorption–desorption isotherms as well as the pore-size-distribution curves of the WO_3 nanoplate and In_2O_3@WO_3(In/W=0.8) composite. One can see that the WO_3 nanoplates and In_2O_3@WO_3 (In/W=0.8) composite show a similar type II isotherm with no obvious hysteresis, suggesting that the samples obtained are a non-porous or macroporous adsorbents.[49] The BET surface areas of the WO_3 nanoplates and In_2O_3@WO_3 (In/W=0.8) composite are 202 $m^2 g^{-1}$ and 224 $m^2 g^{-1}$, respectively. The BET surface area of the In_2O_3@WO_3 composite is higher than that of the WO_3 nanoplates, which is useful to improve the gas-sensing performance.

3.2. Gas-sensing performance

Fig. 6.

We firstly investigated the H_2S-sensing properties of the WO_3 nanoplates and the In_2O_3@WO_3 nanocomposites with various amounts of In_2O_3 contents (In/W=0.5–1). Fig. 6a shows the typical H_2S-sensing (*U*–*t*) profiles of the In_2O_3@WO_3 sensors operating at 150 ^oC upon exposure to the H_2S gases with concentrations of 0.5, 1, 2, 5 and 10 ppm. One can find there are sharp rises and drops in *U* values when the H_2S gas are injected and discharged, respectively, indicating that the In_2O_3@WO_3 sensors are highly sensitive to low-concentration H_2S gases and the resistances of the sensors decrease upon exposure to H_2S gases. The plots of the response (R_a / R_g) of the sensors dependent on the concentration of H_2S gases ([H_2S] / ppm) are shown in Fig. 6b. When the H_2S concentration increases from 0.5 ppm to 10 ppm, the responses of the In_2O_3@WO_3 sensors sharply increase. For a given [H_2S] value, the responses of the In_2O_3@WO_3 sensors increase with the increase in the In_2O_3 amounts from 0 to In/W=0.8, and then decrease when the In_2O_3 NPs amount reaches to In/W=1. The In_2O_3@WO_3(In/W=0.8) sensor presents the highest response upon exposure to H_2S gases with varies concentrations operating at 150 ^oC. Typically, the response of In_2O_3@WO_3(In/W=0.8) sensor upon exposure to 10 ppm H_2S gas can reach more than 143, which is 4 times higher than that (36) of the WO_3 nanoplate sensor. The In_2O_3-dependent gas-sensing performance may be due to the difference in particle sizes and amounts of In_2O_3 NPs.

Fig. 7.

To better understand the gas sensing property of the In_2O_3@WO_3 composites, we have also synthesized In_2O_3 nanoparticles and investigated its gas-sensing performance to H_2S. The H_2S-sensing responses of the sensors derived from the WO_3 nanoplates, In_2O_3@WO_3(In/W=0.8) composite and In_2O_3 nanocrystals are comparatively investigated. Fig. 7 shows the plots of the response versus operation temperatures upon exposure to 10 ppm H_2S gases at a temperature range of 100–250 ^oC. One can see that the WO_3 nanoplates and In_2O_3@WO_3 sensors have maximum responses for H_2S gas at around 150 ^oC, and their responses are 36 and 143, respectively. The pure In_2O_3 sensor shows a sensitivity of 14 to 10 ppm H_2S at 100 ^oC, and its response decreases with the increase in operating temperatures from 100 to 250 ^oC. The responses of the In_2O_3@WO_3 nanocomposite sensors are much higher than those of the WO_3 nanoplate and In_2O_3 nanocrystal sensors, indicating that there is a synergistic effect in improving the H_2S-sensing performance. The In_2O_3@WO_3 (In/W=0.8) sensor has a higher response than those of the other In_2O_3@WO_3 sensors tested from 100 to 250 ^oC. When the operation temperature decreases to 100 ^oC, the In_2O_3@WO_3 sensors show a sharply drop response. The WO_3 nanoplates and In_2O_3@WO_3 sensors therefore have an optimum operating temperature at about 150 ^oC, and too low or too high operation temperature is unfavorable in H_2S-sensing performance of the In_2O_3@WO_3 sensors.

Fig. 8.

Fig. 8 shows the response and recovery times of the WO_3 nanoplate, In_2O_3@WO_3(In/W=0.8) and In_2O_3 nanoparticle sensors upon exposure to 5 ppm H_2S at various operating temperatures (100–250 ^oC). One can easily find that high operating temperatures are helpful to shorten the response and recovery times. The response and recovery times of the In_2O_3@WO_3 sensor at 100 ^oC are 5.5 and 16 min, respectively, whereas the response and recovery times decrease to below 95 s when the operation temperature is 250 ^oC. At the same operating temperature, the response speed of the In_2O_3@WO_3 sensor is much faster than that of the WO_3 nanoplate sensor (Fig. 8a). The existence of In_2O_3 NPs is useful for rapid response, indicating that the hierarchical In_2O_3@WO_3 nanostructure sensor can provide efficient diffusion paths and adsorption sites for the target gas molecules. However, the recovery time of In_2O_3@WO_3 sensor is longer than that of the WO_3 nanoplate sensor, and

the different change trends in recovery times may be due to the special hierarchical microstructure of the In_2O_3@WO_3 composites.

Fig. 9.

To further confirm the selectivity of the In_2O_3@WO_3 sensors, we choose H_2, CH_4, CO, SO_2, acetone, ethanol, isopropanol, methanol, methanol and benzene as the target gases or vapors to conduct the selective gas-sensing tests (Fig. 9). As Fig. 9 shows, one can find that the WO_3 nanoplates and In_2O_3@WO_3 sensors show high responses to H_2S gas at 150 ^oC, whereas the responses to other gases or vapors are very low. The In_2O_3@WO_3 sensor has a higher response than that of the WO_3 nanoplate sensor upon exposure to H_2S under the same test conditions. Whereas the WO_3 nanoplate sensor has a higher response than that of the In_2O_3@WO_3 sensor for the cases of ethanol, isopropanol, methanol, methanol, acetone, benzene and SO_2 under the similar test conditions. To the gases and organic vapors except H_2S, both the WO_3 nanoplate and In_2O_3@WO_3 sensors have low responses (e.g., 1–13). Therefore, the In_2O_3@WO_3 sensor is suitable for H_2S detection at low operating temperature (e.g., less than 150 ^oC) due to its high response and selectivity to H_2S gas. The enhanced response and selectivity to H_2S gas make the In_2O_3@WO_3 nanocomposites potential materials in practical gas-detection applications.

3.3 Possible H_2S-sensing mechanism

Fig. 10.

WO_3 and In_2O_3 are resistive-type gas-sensing materials, and the surface interaction between adsorbed oxygen and the target gas is a key factor influencing their gas-sensing performance.[2] In air, oxygen molecules are adsorbed onto the surfaces of the WO_3 and In_2O_3, and then transferred to O^-, O^{2-} or O_2^- ions by gaining electrons from the conductive bands of WO_3 and In_2O_3, forming electron depletion layers with a high-resistance state (process 1 in Fig. 10). When the In_2O_3@WO_3 sensor is exposed to H_2S gas, H_2S reacts with the oxygen adsorbates (O^-, O^{2-}or O_2^- ions), decreasing the oxygen concentration (Eqs. 1-2). These reactions release electrons that decrease the resistance of the In_2O_3@WO_3 sensor, shown as process 2 and 3 in Fig. 10, forming a low-resistance state. As the operating temperature increases, a higher response is observed because of the enhanced activity of adsorbed

molecular oxygen and lattice oxygen in process 1. This phenomenon continues up to a certain optimum temperature, beyond which exothermic gas adsorption becomes difficult and gas molecules begin to desorb in large quantities, leading to a drop in sensor response.[50] Thus, the optimum temperature is a balance point between the two conflicting aspects of adsorption and activity.

$$H_2S + 3O^-(ads) \rightarrow H_2O + SO_2 + 3e^- \quad (1)$$

$$H_2S + 3O^{2-}(ads) \rightarrow H_2O + SO_2 + 6e^- \quad (2)$$

The enhancement of H_2S-sensing performance of the In_2O_3@WO_3 sensor can be attributed to the synergistic effect of two-dimensional WO_3 nanoplates and zero-dimensional In_2O_3 NPs. On the one hand, the hierarchical configuration of In_2O_3 NPs on WO_3 nanoplates can prevent the aggregation of the In_2O_3 NPs and increase efficient paths for diffusion and adsorption of the target gas molecules. On the other hand, the hetero-junctions at the interface of In_2O_3 and WO_3 can generate a special electron donor-acceptor system.[11] Upon exposure to reducing H_2S gas, the conductivity of the In_2O_3@WO_3 sensor increases, and thus more electrons migrate to accelerate the formation of electron depletion regions that improve the gas-sensing performance. Although the exact mechanism for H_2S-sensing enhancement in the In_2O_3@WO_3 system is not available to date, the synergistic effect of the In_2O_3 and WO_3 species with different dimensions can be essential factors to improve the low-temperature gas-sensing performance of the WO_3-based materials.

Conclusions

The In_2O_3-modified WO_3 nanoplate nanocomposites have been synthesized via a microwave-assisted method. The In_2O_3 NPs uniformly immobilized on the surface of WO_3 nanoplates. The In_2O_3@WO_3 nanocomposite is particularly active and selective toward H_2S. The sensor derived from In_2O_3@WO_3 nanocomposites with a molar In/W ratio of 0.8 shows a high response of 143 upon exposure to 10 ppm H_2S operating at a low temperature of 150 ^oC, and its sensitivity is 4 times higher than that of the WO_3 nanoplates sensor. The improved selectively sensitive of In_2O_3@WO_3 sensors to H_2S gas at low temperature is mainly own to the synergistic effect of the In_2O_3 and WO_3 species.

Acknowledgments

This work was partly sponsored by National Natural Science Foundation of China (51172211, 512101207, 51172213), China Postdoctoral Science Foundation (2013M531682, 2014T70682), Foundation for University Young Key Teacher by Henan Province (2011GGJS-001), Program for Science & Technology Innovation Talents in Universities of Henan Province (14HASTIT011), Special Support Program for High-End Talents of Zhengzhou University (ZDGD13001), and Technology Foundation for Selected Overseas Chinese Scholar (Ministry of Human Resources and Social Security).

References

1 E. Comini, C. Baratto, G. Faglia, M. Ferroni, A. Vomiero, G. Sberveglieri, *Prog. Mater. Sci.*, 2009, 54,1-67.

2 K. Wetchakun, T. Samerjai, N. Tamaekong, C. Liewhiran, C. Siriwong, V. Kruefu, A. Wisitsoraat, A. Tuantranont, S. Phanichphant, *Sens. Actuators B: Chem.*, 2011, 160, 580-591.

3 M.M. Arafat, B. Dinan, S.A. Akbar, A.S.M.A. Haseeb, *Sensors*, 2012, 12, 7207-7258.

4 J.H. Lee, Sens. Actuators B: Chem., 2009, 140, 319-336.

5 N. Singh, R.K. Gupta, P.S. Lee, *ACS Appl. Mater. Interfaces*, 2011, 3, 2246-2252.

6 M. Rumyantseva, V. Kovalenko, A. Gaskov, E. Makshina, V. Yuschenko, I. Ivanova, A. Ponzoni, G. Faglia, E. Comini, *Sens. Actuators B: Chem.*, 2006, 118, 208-214.

7 A. Sharma, M. Tomar, V. Gupta, *Sens. Actuators B: Chem.*, 2013, 176, 675-684.

8 P.-G. Su, Y.-T. Peng, *Sens. Actuators B: Chem.*, 2014, 193, 637-643.

9 Y. Wang, S. Wang, Y. Zhao, B. Zhu, F. Kong, D. Wang, S. Wu, W. Huang, S. Zhang, *Sens. Actuators B: Chem.*, 2007, 125, 79-84.

10 C.X. Wang, L.W. Yin, L.Y. Zhang, D. Xiang, R. Gao, *Sensors*, 2010, 10, 2088-2106.

11 K. Potje-Kamloth, *Chem. Rev.*, 2008, 108, 367-399.

12 C. Zhao, W. Hu, Z. Zhang, J. Zhou, X. Pan, E. Xie, *Sens. Actuators B: Chem.*, 2014, 195, 486-493.

13 D. Chu, Y.-P. Zeng, D. Jiang, Y. Masuda, *Sens. Actuators B: Chem.*, 2009, 137, 630-636.

14 J. Kim, W. Kim, K. Yong, *J. Phys. Chem. C*, 2012, 116, 15682-15691.

15 L. Xu, R. Zheng, S. Liu, J. Song, J. Chen, B. Dong, H. Song, *Inorg. Chem.*, 2012, 51, 7733-7740.

16 T. Kida, A. Nishiyama, Z. Hua, K. Suematsu, M. Yuasa, K. Shimanoe, *Langmuir,* 2014, 30, 2571-2579.

17 Y. Zhu, X. Su, C. Yang, X. Gao, F. Xiao, J. Wang, *J. Mater. Chem.,* 2012, 22, 13914-13917.

18 L. Wang, J. Deng, T. Fei, T. Zhang, *Sens. Actuators B: Chem.*, 2012, 164, 90-95.

19 M.R. Mohammadi, D.J. Fray, *Sens. Actuators B: Chem.,* 2011, 155, 568-576.

20 C. Cheng, B. Liu, H. Yang, W. Zhou, L. Sun, R. Chen, S.F. Yu, J. Zhang, H. Gong, H. Sun, H.J. Fan, *ACS Nano*, 2009, 3, 3069-3076.

21 L. Han, D. Wang, J. Cui, L. Chen, T. Jiang, Y. Lin, *J. Mater. Chem.,* 2012, 22, 12915-12920.

22 K. Sivula, F.L. Formal, M. Grätzel, *Chem. Mater*., 2009, 21, 2862-2867.

23 S. An, S. Park, H. Ko, C. Lee, *Appl. Phys. A-Mater. Sci. Process.*, 2012, 108, 53-58.

24 W. Wu, S. Zhang, X. Xiao, J. Zhou, F. Ren, L. Sun, C. Jiang, *ACS Appl. Mater. Interfaces,* 2012, 4, 3602-3609.

25 M. Bao, Y. Chen, F. Li, J. Ma, T. Lv, Y. Tang, L. Chen, Z. Xu, T. Wang, *Nanoscale*, 2014 6, 4063-4066.

26 X. Xue, L. Xing, Y. Chen, S. Shi, Y. Wang, T. Wang, *J. Phys. Chem. C,* 2008, 112, 12157-12160.

27 Y. J. Zhu, F. Chen, *Chem. Rev.*, 2014, 114, 6462-6555.

28 T. Stoycheva, F.E. Annanouch, I. Gràcia, E. Llobet, C. Blackman, X. Correig, S. Vallejos, *Sens. Actuators B: Chem.*, 2014, 198, 210-218.

29 Z.F. Liu, M. Miyauchi, T. Yamazaki, Y.B. Shen, *Sens. Actuators B: Chem.*, 2009, 140, 514-519.

30 N.S. Ramgir, C.P. Goyal, P.K. Sharma, U.K. Goutam, S. Bhattacharya, N. Datta, M. Kaur, A.K. Debnath, D.K. Aswal, S.K. Gupta, *Sens. Actuators B: Chem.*, 2013, 188, 525-532.

31 S. Bai, K. Zhang, L. Wang, J. Sun, R. Luo, D. Li, A. Chen, *J. Mater. Chem. A*, 2014, 2, 7927-7934.

32 C.S. Rout, M. Hegde, C.N.R. Rao, *Sens. Actuators B: Chem.,* 2008, 128, 488-493.

33 J.T. McCue, J.Y. Ying, *Chem. Mater.,* 2007, 19, 1009-1015.

34 V.D. Kapse, S.A. Ghosh, G.N. Chaudhari, F.C. Raghuwanshi, *Talanta*, 2008, 76,

610-616.

35 M. Kaur, N. Jain, K. Sharma, S. Bhattacharya, M. Roy, A.K. Tyagi, S.K. Gupta, J.V. Yakhmi, *Sens. Actuators B: Chem.*, 2008, 133, 456-461.

36 L. Xu, H. Song, B. Dong, Y. Wang, J. Chen, X. Bai, *Inorg. Chem.*, 2010, 49, 10590-10597.

37 L.G. Bloor, J. Manzi, R. Binions, I.P. Parkin, D. Pugh, A. Afonja, C.S. Blackman, S. Sathasivam, C.J. Carmalt, *Chem. Mater.*, 2012, 24, 2864-2871.

38 X. Lai, D. Wang, N. Han, J. Du, J. Li, C. Xing, Y. Chen, X. Li, *Chem. Mater.*, 2010, 22, 3033-3042.

39 S. Wang, B. Xiao, T. Yang, P. Wang, C. Xiao, Z. Li, R. Zhao, M. Zhang, *J. Mater. Chem. A*, 2014, 2, 6598-6604.

40 P.G. Su, W. Ren-Jang, N. Fang-Pei, *Talanta*, 2003, 59, 667-672.

41 G.N. Chaudhari, A.M. Bende, A.B. Bodade, S.S. Patil, S.V. Manorama, *Talanta*, 2006, 69, 187-191.

42 D. Chen, L. Gao, A. Yasumori, K. Kuroda, Y. Sugahara, *Small*, 2008, 4, 1813-1822.

43 D. Chen, L. Yin, L. Ge, B. Fan, R. Zhang, J. Sun, G. Shao, *Sens. Actuators B: Chem.*, 2013, 185, 445-455.

44 D. Chen, Y. Sugahara, *Chem. Mater.*, 2007, 19, 1808-1815.

45 D. Chen, X. Hou, T. Li, L. Yin, B. Fan, H. Wang, X. Li, H. Xu, H. Lu, R. Zhang, J. Sun, *Sens. Actuators B: Chem.*, 2011, 153, 373-381.

46 D. Chen, X. Hou, H. Wen, Y. Wang, H. Wang, X. Li, R. Zhang, H. Lu, H. Xu, S. Guan, J. Sun, L. Gao, *Nanotechnology*, 2010, 21, 035501.

47 J. Ba, D. Fattakhova Rohlfing, A. Feldhoff, T. Brezesinski, I. Djerdj, M. Wark, M. Niederberger, *Chem. Mater.*, 2006,18, 2848-2854.

48 L. Yin, D. Chen, B. Fan, H. Lu, H. Wang, H. Xu, D. Yang, G. Shao, R. Zhang, *Mater. Chem. Phys.*, 2013,143, 461-469.

49 K.S.W. Sing, D.H. Everett, R.A.W. Haul, L. Moscou, R.A. Pierotti, J. Rouquerol, & T. Siemieniewska. *Pure & Appl. Chem.*, 1985, 57, 603-619.

50 Z. Li, X. Lai, H. Wang, D. Mao, C. Xing, D. Wang, *J. Phys. Chem. C*, 2009, 113, 2792-2797.

List of Figure Captions

Fig. 1. (a–c) XRD patterns of (a) In_2O_3 nanoparticles, (b) In_2O_3@WO_3(In/W=0.8) nanocomposite and (c) WO_3 nanoplates; (d) the standard pattern of In_2O_3 (JCPDS no. 06-0416), (e) the standard pattern of WO_3 (JCPDS no. 32-1395).

Fig. 2. Typical SEM images of (a) WO_3 nanoplates, (b) In_2O_3 nanoparticles, (c) In_2O_3@WO_3(In/W=0.5), (d) In_2O_3@WO_3(In/W=0.8) and (e) In_2O_3@WO_3(In/W=1); (f) EDS spectrum of In_2O_3@WO_3(In/W=0.8) (The inset is the corresponding SEM image).

Fig. 3. TEM observation of the In_2O_3@WO_3(In/W=0.8) nanocomposite: (a) low-magnification TEM image and (b) high-resolution TEM image. The inset is the corresponding FFT pattern.

Fig. 4. XPS spectra of the In_2O_3@WO_3(In/W=0.8) nanocomposite: (a) a survey scan, (b) W 4f, (c) In 3d and (d) O1s.

Fig. 5 Nitrogen (N_2) adsorption–desorption isotherms of (A) WO_3 nanoplates and (B) In_2O_3@WO_3 (In/W=0.8) composite (Inset: the corresponding BJH pore-size-distribution curves).

Fig. 6. (a) Typical response profiles operating at 150 ^oC upon exposure to H_2S gases with various concentrations and (b) plots of the response dependent on H_2S concentration: (A) WO_3, (B) In_2O_3@WO_3(In/W=0.5), (C) In_2O_3@WO_3(In/W=0.8), and (D) In_2O_3@WO_3(In/W=1).

Fig. 7. Plots of the response dependent on operating temperature (100–250 ^oC) upon exposure to 10 ppm H_2S gas: (A) In_2O_3 nanoparticles, (B) WO_3 nanoplates and (C) In_2O_3@WO_3(In/W=0.8).

Fig. 8. Response and recovery times of the sensors derived from WO_3 nanoplates, In_2O_3@WO_3(In/W=0.8) and In_2O_3 nanoparticles upon exposure to 5 ppm H_2S gas at various operating temperatures (100–250 ^oC).

Fig. 9. Selective response of the WO_3 nanoplates and In_2O_3@WO_3(In/W=0.8) composite upon exposure to various gases and vapors operating at 150 ^oC.

Fig. 10. A schematic demonstration of the adsorption and reaction process of O_2 and H_2S molecules at the interface of the hierarchical In_2O_3@WO_3 nanostructure.

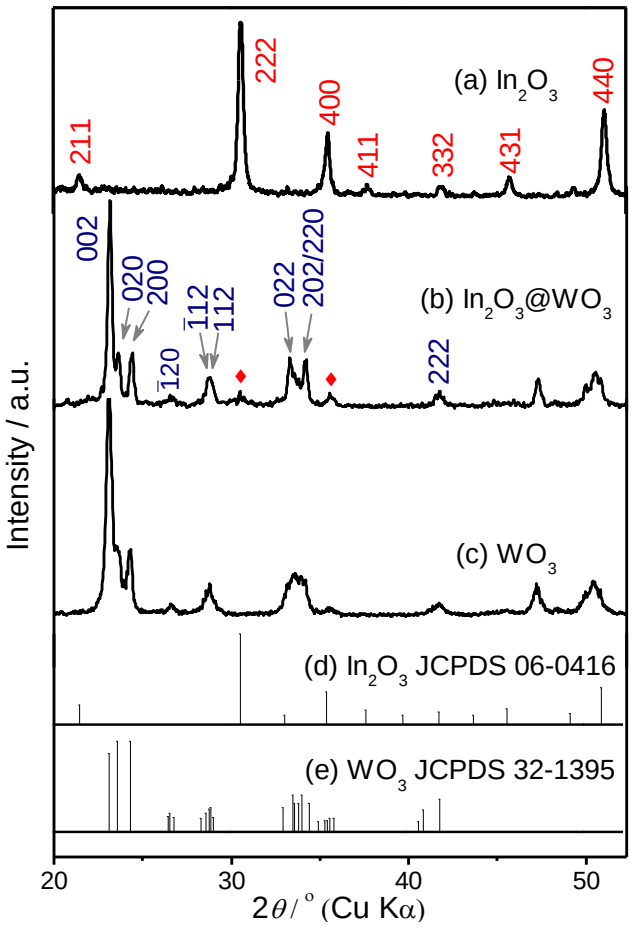

Fig. 1. By L. Yin, D. Chen, and *et al*..

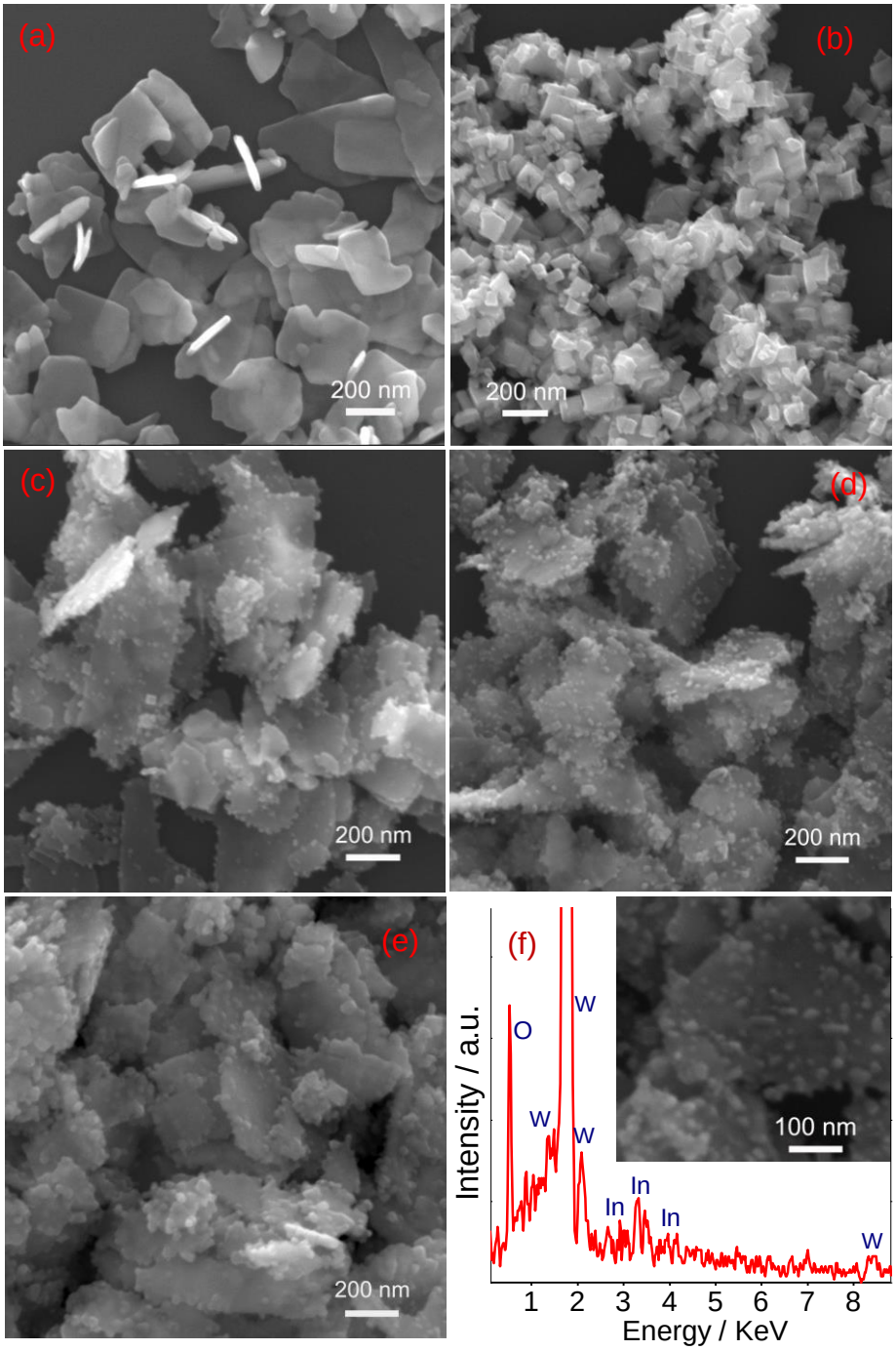

Fig. 2. By L. Yin, D. Chen, and *et al.*.

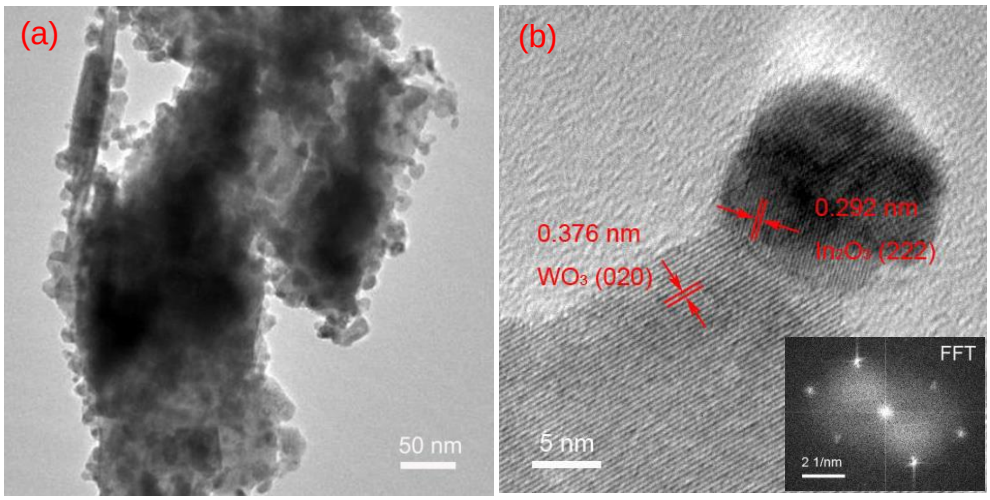

Fig. 3. By L. Yin, D. Chen, and *et al.*.

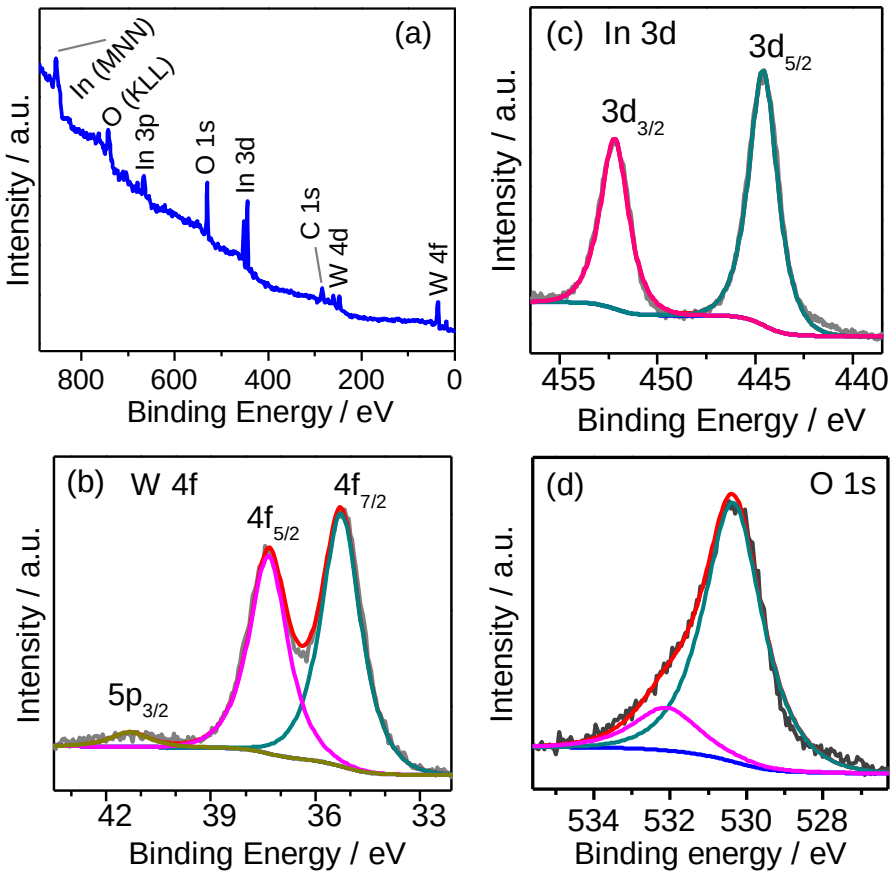

Fig. 4. By L. Yin, D. Chen, and *et al.*.

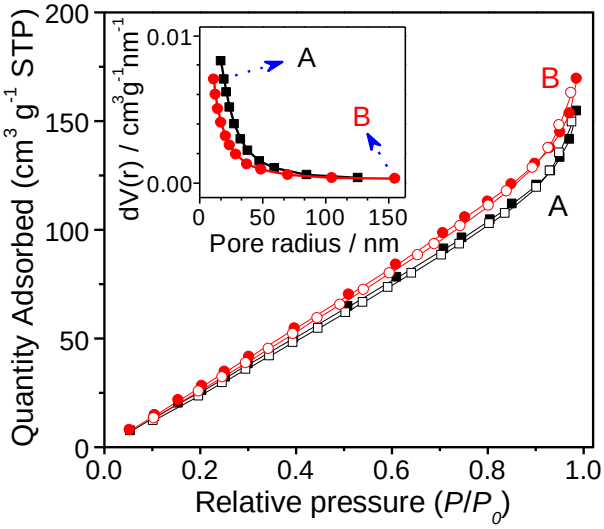

Fig. 5. By L. Yin, D. Chen, and *et al.*.

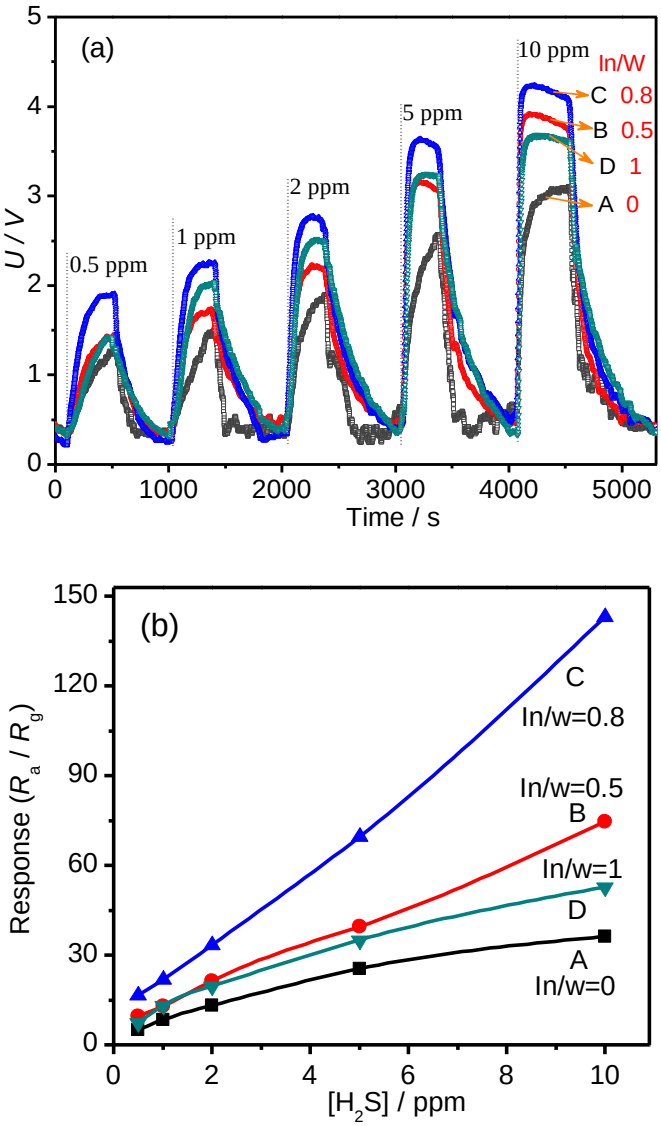

Fig. 6. By L. Yin, D. Chen, and *et al.*.

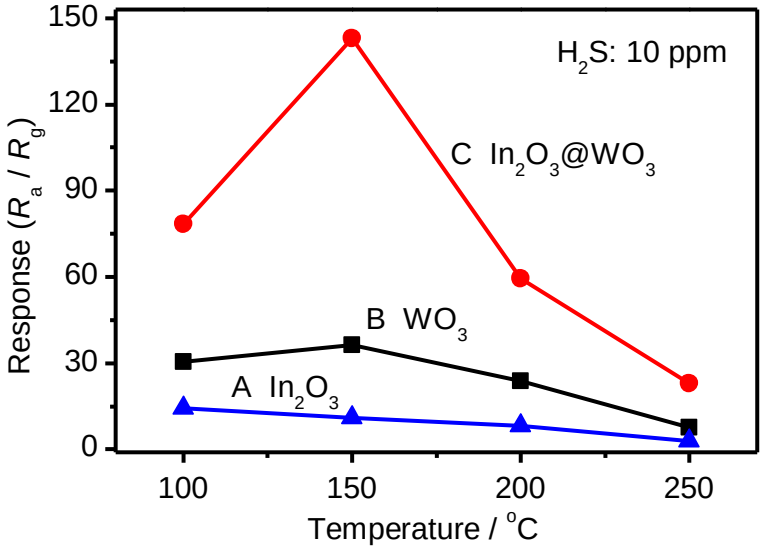

Fig. 7. By L. Yin, D. Chen, and *et al.*.

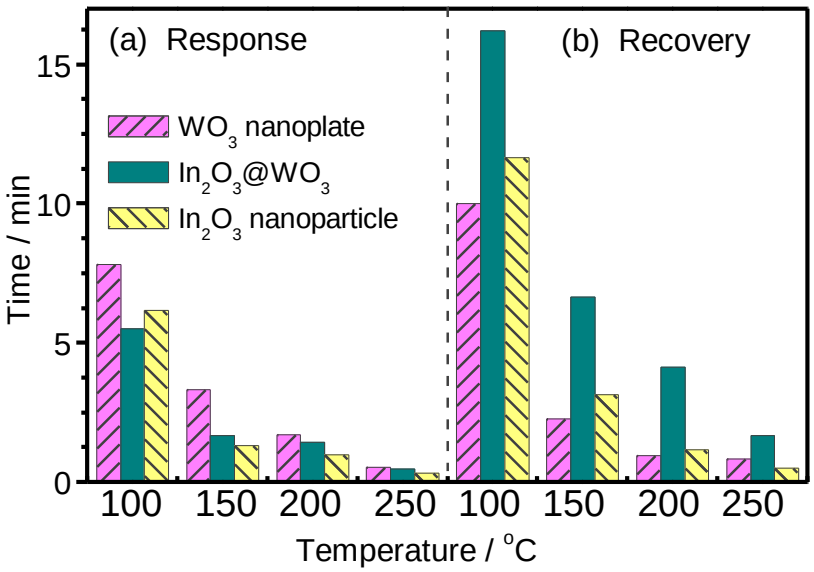

Fig. 8. By L. Yin, D. Chen, and *et al.*.

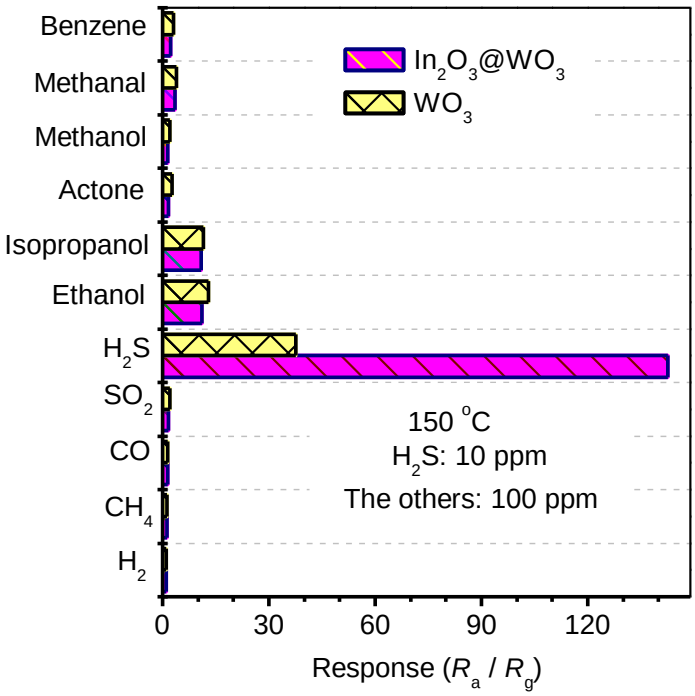

Fig. 9. By L. Yin, D. Chen, and *et al.*.

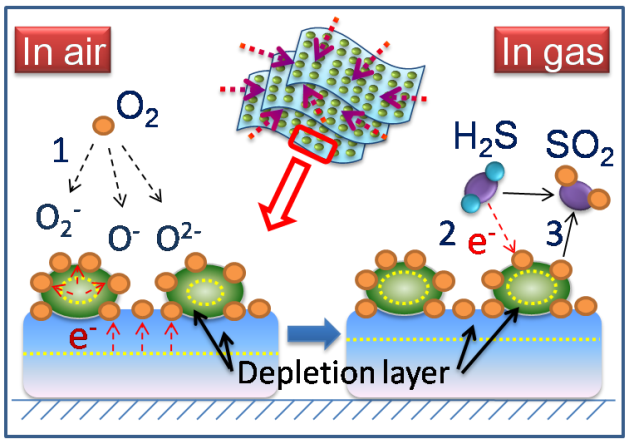

Fig. 10. By L. Yin, D. Chen, and *et al.*.